

# Rise of the First Super-Massive Stars

John A. Regan\* & Turlough P. Downes

*Centre for Astrophysics & Relativity, School of Mathematical Sciences, Dublin City University, Glasnevin, Ireland*

18 May 2018

## ABSTRACT

We use high resolution adaptive mesh refinement simulations to model the formation of massive metal-free stars in the early Universe. By applying Lyman-Werner (LW) backgrounds of 100  $J_{21}$  and 1000  $J_{21}$  respectively we construct environments conducive to the formation of massive stars. We find that only in the case of the higher LW backgrounds are super-critical accretion rates realised that are necessary for super-massive star (SMS) formation. Mild fragmentation is observed for both backgrounds. Violent dynamical interactions between the stars that form in the more massive halo formed (1000  $J_{21}$  background) results in the eventual expulsion of the two most massive stars from the halo. In the smaller mass halo (100  $J_{21}$  background) mergers of stars occur before any multibody interactions and a single massive Pop III star is left at the centre of the halo at the end of our simulation. Feedback from the very massive Pop III stars is not effective in generating a large HII region with ionising photons absorbed within a few thousand AU of the star. In all cases a massive black hole seed is the expected final fate of the most massive objects. The seed of the massive Pop III star which remained at the centre of the less massive halo experiences steady accretion rates of almost  $10^{-2} M_{\odot}/\text{yr}$  and if these rates continue could potentially experience super-Eddington accretion rates in the immediate aftermath of collapsing into a black hole.

**Key words:** Cosmology: theory – large-scale structure – first stars, methods: numerical

## 1 INTRODUCTION

Very high redshift quasars powered by super massive black holes (SMBHs) have presented a problem when trying to reconcile the very large masses of these objects with possible progenitors. The most recent discovery being made by [Bañados et al. \(2017\)](#) of a quasar at  $z = 7.54$  with an estimated mass of  $M = 8 \times 10^8 M_{\odot}$ . This discovery adds to the previous record holder of  $z = 7.085$  ([Mortlock et al. 2011](#)). At the present time there have been more than one hundred quasars discovered at redshifts greater than 6 ([Wang et al. 2016, 2017](#)). The presence of such massive objects at early times in the Universe presents a fundamental problem in terms of the progenitors of these objects.

Stellar mass black holes formed from the remnants of the first stars (Pop III stars) must accrete at the Eddington limit for their entire history to reach the billion mass threshold by a redshift of 7 if they are to be the seeds of the first quasars. This scenario appears exceedingly difficult as the first stellar mass black holes are born “starving” ([Whalen et al. 2004](#); [Alvarez et al. 2009](#); [Johnson et al. 2011](#)) in mini haloes which have been disrupted by both the ionising radiation from Pop III stars and the subsequent supernova explosions ([Milosavljević et al. 2009](#); [Jeon et al. 2014](#)). Furthermore,

the remnants of Pop III stars continue to accrete very inefficiently even after migrating into larger haloes via mergers ([Smith et al. in prep](#)). As a direct result, investigation of supermassive star (SMS) formation as a viable alternative has been undertaken and appears attractive ([Haiman 2006](#); [Begelman et al. 2006](#); [Wise et al. 2008](#); [Regan & Haehnelt 2009a,b](#); [Volonteri 2010](#); [Agarwal et al. 2012, 2013, 2014](#); [Latif & Volonteri 2015](#); [Latif et al. 2016](#); [Regan et al. 2017](#)).

Recent work on the formation of SMSs ([Woods et al. 2017](#); [Haemmerlé et al. 2018, 2017](#); [Hosokawa et al. 2016, 2013a,b](#)) has come to the broad consensus that when proto-stars are subject to accretion rates greater than approximately  $0.04 M_{\odot}/\text{yr}$  the envelope surrounding the proto-star becomes bloated leading to effective surface temperatures of approximately 5000 K. SMSs are therefore expected to resemble red giants albeit with significantly more luminosity. Using 2-D hydrodynamical simulations [Sakurai et al. \(2016\)](#) show that even in the case when the accretion rate onto the proto-star drops below the critical accretion rate the resulting UV feedback is too weak to halt accretion as long as the periods of quiescence are less than approximately 1000 years. SMSs are then expected to continue accreting until they directly collapse into a black hole with initial masses of approximately  $M_{\text{BH}} \sim 10^5 M_{\odot}$ .

Creating the conditions for generating these extreme accretion rates has therefore been a topic of great interest to astrophysicists

\* E-mail:john.regan@dcu.ie, Marie Skłodowska-Curie Fellow

**Table 1.** Simulation Parameters

<i>Sim Name</i> <sup>a</sup>	$J_{21}^b$	<i>Maximum Resolution</i> <sup>c</sup> (pc)	<i>Collapse Redshift</i> <sup>d</sup>	$M_{\text{core}}^f$ ( $M_{\odot}$ )	$M_{\text{halo}}^g$ ( $M_{\odot}$ )
Ref18_1J	1	0.001	27.1	7740	$9.56 \times 10^6$
Ref10_100J	100.0	0.44	$z = 24.7$	16866	$1.38 \times 10^7$
Ref14_100J21	100.0	0.02	$z = 24.7$	16462	$1.38 \times 10^7$
Ref18_100J21	100.0	0.001	$z = 24.7$	21194	$1.39 \times 10^7$
Ref20_100J21_OT	100.0	0.00025	$z = 24.7$	21187	$1.39 \times 10^7$
Ref14_1000J21	1000.0	0.02	$z = 23.7$	58948	$2.67 \times 10^7$
Ref16_1000J21	1000.0	0.004	$z = 23.7$	59018	$2.67 \times 10^7$
Ref18_1000J21_OT	1000.0	0.001	$z = 23.7$	59921	$2.59 \times 10^7$

*Notes:* The details of each of the realisations used in this study. (a) The simulation name, (b) The LW intensity in units of  $J_{21}$ , (c) the maximum physical resolution, (d) the collapse redshift (i.e. the redshift at which the first smartstar forms), (f) gas mass within the central 1 pc just before the first SmartStar forms (g) is the halo virial mass (DM & gas) in solar masses.

over the last decade or more. In the course of the “normal” collapse of structure, metal-free stars made entirely of Hydrogen and Helium form with typical accretion rates of  $M_{\text{acc}} \lesssim 10^{-3} M_{\odot}/\text{yr}$ . Accretion rates of this magnitude do not lead to SMS formation but rather the formation of Population III stars which are extremely luminous in the UV. The feedback from the creation of the Pop III star effectively halts accretion and is expected to set a characteristic mass of approximately 40 solar masses for Pop III stars (Hosokawa et al. 2011; Hirano et al. 2014; Hosokawa et al. 2016). However, as noted above black hole progenitors beginning with initial masses of this magnitude must accrete at the Eddington rate for approximately a billion years in order to achieve the masses required of the first quasars.

As a result of the early bottlenecks likely suffered by the first stars in terms of their growth prospects many authors have considered the idea that SMSs may be a more natural progenitor for the first quasars. Their significantly increased initial masses alleviates some of the difficulties in achieving final masses of a billion solar masses within a gigayear timeframe. The very high accretion rates required to form a SMS requires larger halos than those in which normal Pop III star formation occurs. If star formation can be suppressed until a dark matter halo reaches the atomic cooling threshold then the accretion rates onto a central object can reach rates of nearly  $1 M_{\odot}/\text{yr}$  - well in excess of the critical rate required. The conditions required to form pristine atomic cooling haloes has been investigated by several authors over the past decade or more. As Pop III stars form they emit copious amounts of Lyman-Werner (LW) radiation. LW photons can dissociate  $\text{H}_2$  thus removing a crucial coolant that allows Pop III star formation to proceed. If the LW flux impinging onto a growing halo is large enough then Pop III star formation can be completely suppressed until the atomic cooling limit is reached at which point cooling by atomic hydrogen drives the collapse. This mechanism by which external (LW) radiation from one (or more) star forming haloes sterilises a neighbouring halo also requires that the target halo remains metal-free. As a result the term “synchronised” haloes has been coined (Dijkstra et al. 2008; Agarwal et al. 2014; Dijkstra et al. 2014; Visbal et al. 2014; Regan et al. 2017).

Another promising avenue to achieving the required accretion rates in pristine haloes is in haloes that are exposed to large streaming velocities (Tseliakhovich & Hirata 2010). In this case the large offset in velocities between the dark matter particles and the baryons suppresses the ability of the halo to virialise until its mass exceeds the atomic cooling threshold. Streaming velocities therefore also suppress Pop III star formation in minihaloes. In this case it has been shown that as the halo collapses it forms  $\text{H}_2$  but the

accretion rates are so high that SMS formation may nonetheless result (Hirano et al. 2017). Schauer et al. (2017) showed that streaming velocities may also provide ideal sites for synchronization of haloes to take place with the first proto-galaxy to collapse effectively sterilising the second galaxy promoting the formation of a SMS.

In this study we explore the formation of a massive proto-star when exposed to large LW backgrounds. The LW background allows us to suppress the formation of Pop III stars in minihaloes in our volume with collapse only able to proceed once atomic cooling becomes important. We use star particles to follow the evolution of proto-star formation. We explicitly track the accretion onto the star particles and investigate if accretion rates above the critical threshold can be sustained over the 1 Myr expected lifetime of the proto-star. At the end of its life the massive star directly collapses into a black hole. In a companion paper we investigate the initial growth of the embryonic black hole under different accretion and feedback regimes.

The paper is laid out as follows: in §2 we describe the model setup and the numerical approach used as well as describing our star particle formulation; in §3 we describe the results of our numerical simulations; in §4 we discuss the importance of the results and present our conclusions.

Throughout this paper we assume a standard  $\Lambda$ CDM cosmology with the following parameters (Planck Collaboration et al. 2014, based on the latest Planck data),  $\Omega_{\Lambda,0} = 0.6817$ ,  $\Omega_{\text{m},0} = 0.3183$ ,  $\Omega_{\text{b},0} = 0.0463$ ,  $\sigma_8 = 0.8347$  and  $h = 0.6704$ . We further assume a spectral index for the primordial density fluctuations of  $n = 0.9616$ .

## 2 NUMERICAL FRAMEWORK

In this study we have used the publicly available adaptive mesh refinement code Enzo<sup>1</sup> to study the fragmentation properties of gas within haloes irradiated by a background LW field. Into Enzo we have added a new star particle type which we have dubbed SmartStar. We now describe both components.

### 2.1 Enzo

Enzo<sup>2</sup> (Bryan et al. 2014) is an adaptive mesh refinement code ideally suited for simulations of the high redshift uni-

<sup>1</sup> <http://enzo-project.org/>

<sup>2</sup> Changeset:fedb30ff370b

verse. Gravity in `Enzo` is solved using a fast Fourier technique (Hockney & Eastwood 1988) which solves the Poisson equation on the root grid at each timestep. On subgrids, the boundary conditions are interpolated to the subgrids and the Poisson equation is then solved at each timestep. Dark matter is represented using particles, each particle is stored on the highest refinement grid available to it and thus the particle has the same timestep as the gas on that grid. The particle densities are interpolated onto the grid and solved at the same time as the gas potential. `Enzo` contains several hydrodynamics schemes to solve the Euler equation. We use the piecewise parabolic method which was originally developed by Berger & Olinger (1984) and adapted to cosmological flows by Bryan et al. (1995). The PPM solver is an explicit, higher order accurate version of Godunov’s method for ideal gas dynamics with a spatially third accurate piecewise parabolic monotonic interpolation scheme employed. A nonlinear Riemann solver is used for shock capturing. The method is formally second order accurate in space and time and explicitly conserves mass, linear momentum and energy making the scheme extremely useful for following the collapse of dense structures.

Chemistry is an important component in following the collapse of (ideal) gas. We use the `Grackle`<sup>3,4</sup> (Smith et al. 2017) library to follow the evolution of ten individual species:  $\text{H}$ ,  $\text{H}^+$ ,  $\text{He}$ ,  $\text{He}^+$ ,  $\text{He}^{++}$ ,  $\text{e}^-$ ,  $\text{H}_2$ ,  $\text{H}_2^+$ ,  $\text{H}^-$  and  $\text{HeH}^+$ . We adopt here the 26 reaction network determined by Glover (2015a) as the most appropriate network for solving the chemical equations required by gas of primordial composition with no metal pollution and exposed to an external radiation source. The network includes the most up-to-date rates as described in Glover & Jappsen (2007), Glover & Abel (2008), Glover & Savin (2009), Coppola et al. (2011), Coppola et al. (2012), Glover (2015a), Glover (2015b), Latif et al. (2015). The cooling mechanisms included in the model are collisional excitation cooling, collisional ionisation cooling, recombination cooling, bremsstrahlung and Compton cooling off the CMB.

## 2.2 Simulation Setup

The simulation volumes considered here are designed to explore the collapse of a single cosmological halo with no metals. External LW backgrounds are used to suppress  $\text{H}_2$  formation leading to the formation of pristine atomic cooling haloes. We now describe the details of the setup. All simulations are run within a cosmological box of  $2 h^{-1}$  Mpc (comoving), the root grid size is  $256^3$  and we employ three levels of nested grids. The grid nesting and initial conditions were created using MUSIC (Hahn & Abel 2011). Within the most refined region (i.e. level 3) the dark matter particle mass is  $\sim 103 M_\odot$ . In order to increase further the dark matter resolution of our simulations we split the dark matter particles according to the prescription of Kitsionas & Whitworth (2002) and as described in Regan et al. (2015). We split particles centered on the position of the final collapse as found from lower resolution simulations within a region with a comoving side length of  $43.75 h^{-1}$  kpc. Each particle is split into 13 daughter particles resulting in a final high resolution region with a dark matter particle mass of  $\sim 8 M_\odot$ . The particle splitting is done at a redshift of 40 well before the collapse of the target halo. Convergence testing to study the impact

of lower dark matter particle masses was discussed in Regan et al. (2015).

The baryon resolution is set by the size of the grid cells. In the highest resolution region this corresponds to approximately  $0.48 h^{-1}$  kpc comoving (before adaptive refinement). We vary the maximum refinement level (see Table 1) to explore the impact of resolution on our results. Refinement is triggered in `Enzo` when certain, user defined, thresholds are exceeded. The refinement criteria used in this work were based on three physical measurements: (1) The dark matter particle over-density, (2) The baryon over-density and (3) the Jeans length. The first two criteria introduce additional meshes when the over-density of a grid cell with respect to the mean gas or dark matter density exceeds 8.0. Furthermore, we set the *MinimumMassForRefinementExponent* parameter to  $-0.1$  making the refinement more aggressive for the baryon and dark matter over-density and hence making the behaviour of the adaptive mesh “super-Lagrangian” in nature (see Bryan et al. (2014) for further details). This technique also reduces the threshold for refinement as higher densities are reached. For the final criteria we set the number of cells per Jeans length to be 32 in these runs.

We use between 10 and 20 levels of refinement in our simulations. A refinement level of 10 corresponds to a comoving spatial resolution  $\Delta x_c \sim 10$  pc and a physical resolution of  $\Delta x_p \sim 0.4$  pc at  $z = 25$ . A refinement level of 20 on the other hand reduces our spatial resolution to  $\Delta x_c \sim 0.01$  pc (comoving) and a physical resolution of  $\Delta x_p \sim 0.0004$  pc ( $\sim 90$  AU) at  $z = 25$ . At this resolution scale we are able to marginally resolve the formation of individual SMSs. In order to suppress Pop III star formation and allow the simulation to form pristine atomic cooling haloes we impose an artificial Lyman-Werner background. We set the effective temperature of the background radiation field to  $T_{\text{eff}} = 30000$  K. This background temperature suitably models the spectrum of a population of young stars (Wolcott-Green & Haiman 2012; Sugimura et al. 2014; Latif et al. 2015). The effective temperature of the background is important as the radiation temperature determines the dominant photo-dissociation reaction set in the irradiated halo. This in turn leads to a value of  $J_{\text{crit}}$  - the flux above which complete isothermal collapse of the irradiated halo is observed due to the complete suppression of  $\text{H}_2$ . The actual value of  $J_{\text{crit}}$  depends on the nature of the source spectrum (Shang et al. 2010; Sugimura et al. 2014; Agarwal & Khochfar 2015). We do not investigate the exact value of  $J_{\text{crit}}$  here in SMS formation, rather we use the LW background as a mechanism to form atomic cooling haloes in which to probe SMS formation and evolution.

## 2.3 Smart Stars

As the gas density increases in high density regions, hydro codes, including `Enzo`, require a method to convert the high density gas into stars in many cases. This is done to deal with gas which has reached the maximum allowed refinement level of the simulation and for which further collapse is being artificially suppressed through artificial pressure support. Gas which has reached this point is expected to result in star formation and so star particles are introduced. In this work we introduce particles to mimic the formation of both Pop III stars and SMSs. Upon formation all stars are assumed to be stars with low surface temperatures that are appropriate for main sequence SMSs and less massive proto-stars on the Hayashi track. Rapidly accreting (i.e.  $\dot{M}_* \gtrsim 0.04 M_\odot/\text{yr}$ ) proto-stars carry large amounts of entropy (hot accretion) into the stellar interior. The stellar radius monotonically increases

<sup>3</sup> <https://grackle.readthedocs.org/>

<sup>4</sup> Changeset:482876c71f73

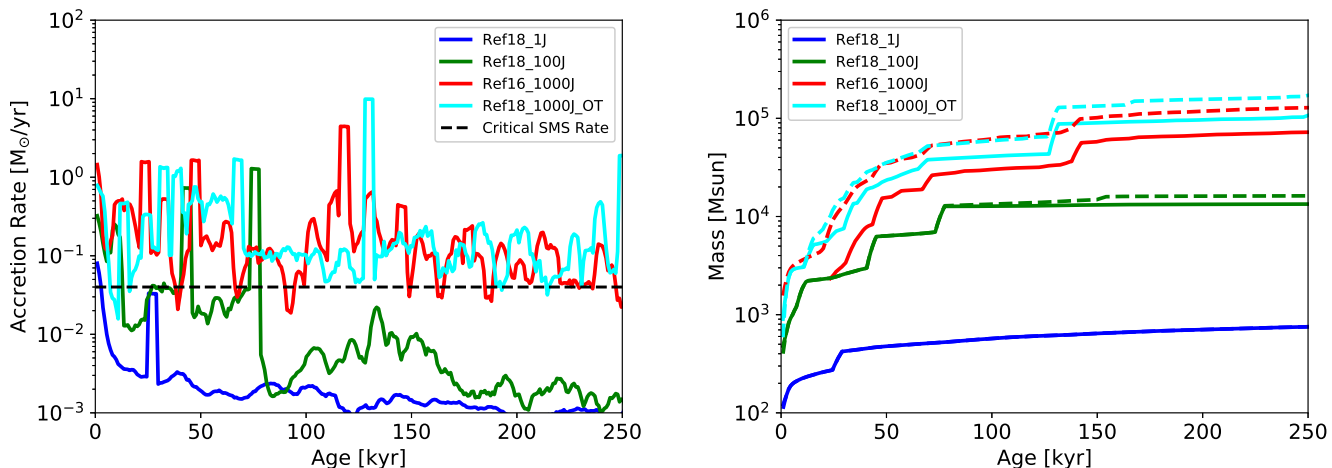


**Figure 1.** The mass accretion rate onto the largest *SmartStar* particle in the simulation with a maximum refinement level of 18 (corresponding to a spatial resolution of  $\Delta x \sim 0.001$  pc). For the Ref18\_1000J\_OT simulation the radiative transfer is made using the optically thin approximation and so we also include the Ref16\_1000J simulation (with full radiative transfer) for direct comparison. The accretion rates, on average, increase with the intensity of the background as expected. The convergence between the Ref16\_1000J and Ref18\_1000J\_OT results should also be noted. In the right hand panel we show the mass of the largest particle in each case and the total mass of all *SmartStar* particles (dashed line). The 1 J<sub>21</sub> simulation shows the lowest stellar masses with the masses of the most massive stars increasing with background intensity. Again note the excellent convergence between the Ref16\_1000J and Ref18\_1000J\_OT results with differences within a factor of two.

as the stellar mass increases obeying an analytic mass-radius relation (Hosokawa et al. 2010, 2013a,b)

$$R_* \approx 2.6 \times 10^3 R_{\odot} \left( \frac{M_*}{100 M_{\odot}} \right)^{1/2} \quad (1)$$

where  $R_*$  is the stellar radius and  $M_*$  is the stellar mass. Note that the relation is independent of the actual accretion rate. The stellar interior remains inhomogeneous and subsequently contracts radiating energy away. A surface layer containing a small fraction of the mass inflates leading to a puffy SMS with low effective temperatures. The expansion continues until the radius eventually begins to contract when the mass of the star exceeds  $M_* \gtrsim 3 \times 10^4 M_{\odot}$ . This occurs because  $\text{H}^-$  bound-free opacity, which keeps the stellar surface temperature locked at close to 5000 K becomes unavailable as the density in the surface layer drops below  $10^{-11} \text{ g cm}^{-3}$ . Nonetheless, the radius at this stage of its evolution is approximately 100 AU. In the case where the accretion rates are more sedate and less than a critical threshold of  $0.04 M_{\odot}/\text{yr}$  (Sakurai et al. 2016) then the accretion is referred to as cold accretion. The gas contains much less entropy and the radius does not increase monotonically with mass. In this case the stellar evolution is that of a normal Pop III star. In the case of sustained high accretion rates our *SmartStar* remains a SMS. On the otherhand if the rates are detected to fall below the critical threshold then the star automatically converts to a Pop III star reflecting the contraction of the Pop III star to the main sequence on the Kelvin-Helmholtz timescale. The type of the star will determine the radiation feedback from the star. Pop III stars are modelled assuming a blackbody spectrum with an effective temperature of  $T_{\text{eff}} = 10^5 \text{ K}$  (Schaerer 2002) while SMSs are modelled by assuming a blackbody spectrum with an effective temperature of  $T_{\text{eff}} = 5500 \text{ K}$  (Hosokawa et al. 2013b). The luminosity rates for the PopIII star as given by Schaefer (2002) have recently been verified by Haemmerlé et al. (2017) who recover the rates of Schaefer (2002) for cases where the accretion rate is below the critical rate. Nonetheless, including the more recent and

updated rates of Haemmerlé et al. (2017) will be included in future development of the algorithms.

In order to form a *SmartStar* particle we assess the following criteria on every timestep:

- (i) The cell is at the highest refinement level
- (ii) The cell exceeds the Jeans density
- (iii) The flow around the cell is converging along each axis
- (iv) The cooling time of the cell is less than the freefall time
- (v) The cell is at a local minimum of the gravitational potential

The Jeans density is calculated using the prescription given in Krumholz et al. (2004) which itself follows from the Truelove criteria (Truelove et al. 1997, 1998). We calculate the gravitational potential in a region of twice the Jeans length around the cell. We experimented with also including the additional conditions relating to the gas boundedness and the Jeans instability test (see Federrath et al. (2010) for more details). However, we found that these additional tests were sub-dominant compared to the criteria noted above and so in the interest of optimisation we did not include them.

When calculating the velocity of the particles subsequent to accretion events we explicitly invoke conservation of momentum to determine the updated velocity of the particle. Doing so ensures we explicitly conserve linear momentum within the system (Krumholz et al. 2004).

## 2.4 Accretion onto the *SmartStar*

Once a *SmartStar* is formed it can accrete gas within its accretion radius (4 cells) and it can merge with other *SmartStar* particles. Accretion onto the *SmartStar* is determined by calculating the flux of gas across the accretion surface.

$$\dot{M} = 4\pi \int_S \rho v_r^- r^2 dr \quad (2)$$

where  $\dot{M}$  is the mass accretion rate,  $S$  is the surface over which we integrate,  $\rho$  is the density of the cells intersecting the surface,  $v_r^-$  is the velocity of cells intersecting the surface and which have negative radial velocities and  $r$  is the radius of our surface. The surface,  $S$ , is the surface of a sphere with radius the accretion radius. As noted above we set the accretion radius to be 4 cells, we choose to fix this radius independent of the resolution or the mass of the `SmartStar`. We do this so as to be as accurate as possible when calculating the accretion rate, any mass travelling radially inward at a distance of four cells from the `SmartStar` is taken to be accreted onto the `SmartStar` - we therefore strive for the maximum possible physical resolution. For completeness we experimented with increasing the accretion radius up to 64 cells and found only small variations in our accretion rate results. Fragmentation is, however, greatly reduced as `SmartStars` are prevented from forming within the accretion radius of another `SmartStar`. The accretion onto the star is calculated at each timestep, however this is likely to be a very noisy metric. To alleviate this to some degree we average the accretion rate over intervals of 1 kyr and use that averaged accretion rate as the actual accretion rate. The accretion rate is added as an attribute to each star and hence a full accretion history of every `SmartStar` is outputted as part of every snapshot.

Mergers with other `SmartStars` are also included in the accretion onto the `SmartStar`. In this case the more massive `SmartStar` retains its information (i.e. age, type etc) after the merger event - information on the less massive `SmartStar` is lost. The mass of the less massive `SmartStar` is added to the accretion rate of the more massive `SmartStar` for that timestep. `SmartStars` are merged when they come within an accretion radius of each other.

## 2.5 Feedback from the `SmartStar`

Upon formation a `SmartStar` is initially assigned a SMS type. The type of the star is only determined by its mass accretion rate and is independent of the chemical environment. The  $H_2$  fraction is not a criteria for forming stars. In Pop III studies, Pop III stars are generally only formed when the  $H_2$  fraction is greater than  $10^{-4}$  (e.g. O’Shea & Norman 2007). However, since we are primarily concerned with SMS formation in a metal-free context our criteria must be different. If the accretion rate onto the star falls below the critical threshold of  $0.04 M_\odot/\text{yr}$  then the star changes type and becomes a Pop III star (Sakurai et al. 2016). The type of the star determines its feedback. Pop III stars are modelled assuming a blackbody spectrum with a characteristic mass of  $40 M_\odot$  (Table 4, Schaerer (2002)). From that we assign a *LuminosityPerSolar-Mass* to the Pop III star and the star consequently becomes more luminous and the feedback more intense as the mass of the star increases. We allow accretion onto the star in tandem with feedback. Since the spectrum of a Pop III is strong in the UV it will strongly ionise the surrounding medium. However, in regions of very high infall the HII regions of the Pop III star are unable to expand more than a few cells from the star due to the extreme opacity of the surrounding gas (Chon et al. 2018).

SMSs are modelled by assuming a blackbody spectrum with an effective temperature of  $T_{eff} = 5500$  K (Hosokawa et al. 2013b). The radiation spectrum for a SMS therefore peaks in the infrared as opposed to the UV for Pop III stars. For the specific luminosity of the SMS we take a characteristic mass of  $500 M_\odot$  and apply the contribution from the non-ionising photons only (Schaerer 2002). As with the ‘normal’ Pop III stars the SMS luminosity

changes as mass is accreted and the total luminosity then scales up as the mass increases.

In both cases the radiation from the stars is propagated outwards from the star using the `MORAY` radiative transfer package (Wise & Abel 2011) that is part of `ENZO`. `MORAY` is able to model the ionisation of H, He and  $He^+$ . It can also account for the photo-dissociation of  $H_2$  for photons with energies within the Lyman-Werner band and the photo-detachment of  $H^-$  and  $H_2^+$  for photons in the infrared band. For each type of star we use five energy bins. The first two energy bins ( $E < 13.6$  eV) are weighted by the cross section peaks for  $H^-$ ,  $H_2^+$  and  $H_2$  photo detachment/dissociation respectively. The next three energy bins are determined using the `sedop` code developed by Mirocha et al. (2012) which determines the optimum number of energy bins needed to accurately model radiation with energy above the ionisation threshold of hydrogen. For the self-shielding of  $H_2$  against LW radiation we use the prescription of Wolcott-Green et al. (2011).

`MORAY` is also able to switch to an optically thin mode of radiative transfer on demand. For the highest resolution runs this can be especially useful due to the fact that propagating photons through a high density AMR mesh becomes computationally prohibitive. For those cases we include only the feedback in the Infrared and LW bands - which are of most relevance to SMSs and we assume that the radiation from Pop III stars is effectively halted close to the star (which is a reasonable assumption at least in the first 100 kyr (Chon et al. 2018)).

## 3 RESULTS

In Table 1 we detail the simulations carried out in this study. We explore two background cases, one with a LW background of  $100 J_{21}$  and one with a background level of  $1000 J_{21}$ . Furthermore, we run one simulation with a background of  $1 J_{21}$  for completeness but this low level background is unlikely to foster the formation of a SMS. A background with a value of  $1000 J_{21}$  is likely required to drive a fully isothermal collapse where  $H_2$  is fully suppressed throughout the halo. The  $100 J_{21}$  case suppresses  $H_2$  until the core can sufficiently self-shield but regions of the Universe exposed to  $100 J_{21}$  are likely to be much more common compared to  $1000 J_{21}$  (Ahn et al. 2009; Inayoshi & Tanaka 2015) and perhaps offer a more realistic condition for forming the vast majority of SMBH seeds. We begin by examining the accretion rates onto the `SmartStar` particles during their evolution.

### 3.1 Accretion Histories

In the left hand panel of Figure 1 we show the mass accretion history for the largest `SmartStar` particle for four different realisations. We use three different backgrounds  $1 J_{21}$ ,  $100 J_{21}$  &  $1000 J_{21}$ . For each background we show the results from simulations at a maximum refinement level of 18 which corresponds to a spatial resolution of  $0.001$  pc at  $z = 25.5$  ( $\sim 200$  AU). At this resolution we are within an order of magnitude of the accretion disk radius of a SMS. We could push our resolution to higher values but instead we focus on extending the runtimes to a significant fraction of the lifetime of the SMS while also testing for convergence. For the realisation with a background of  $1000 J_{21}$  the computational expense of the run meant that we compromised by using the optically thin (OT) approximation for the radiative transfer as described in §2.5. Simulations run with the optically thin approximation are suffixed with ‘OT’ (e.g. Ref18\_1000J21\_OT in Table 1). We therefore also show

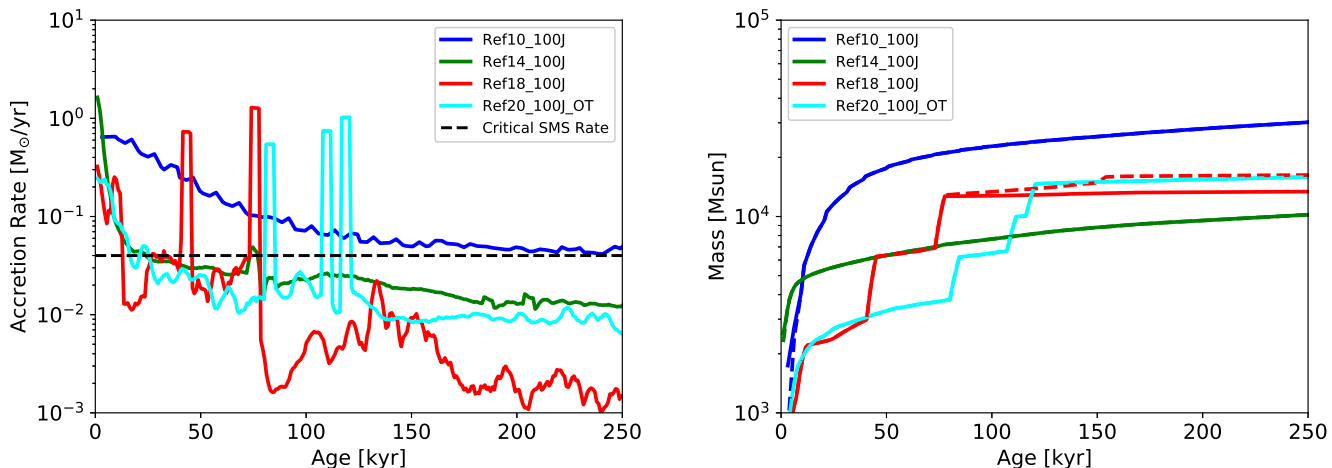


**Figure 2.** The mass accretion rate onto the largest *SmartStar* particle in each simulation for the 100  $J_{21}$  case. The only difference between each simulation is the maximum resolution. As the resolution is increased we see a general trend of decreasing accretion rate. There are several factors at play, firstly the increased resolution allows for the capture of fragmentation within the collapsing gas with competitive accretion ensuing between the (massive) stars. Related to this is the fact that higher resolution leads to clumps being resolved and potentially to a more chaotic accretion pattern as seen in the Ref18 and Ref20 simulations in particular. This is because as the resolution increases we are able to better resolve the small scale structure of the gas surrounding our accretion zone. In the right hand panel we show the mass of the largest particle in each case as well as the cumulative mass of all of the *SmartStar* particles in each simulation. As expected from the mass accretion rates in the left hand panel the Ref10 simulation shows the largest masses. The Ref18 and Ref20 show excellent convergence after approximately 150 kyr but with differences, due to the different accretion histories, before that.

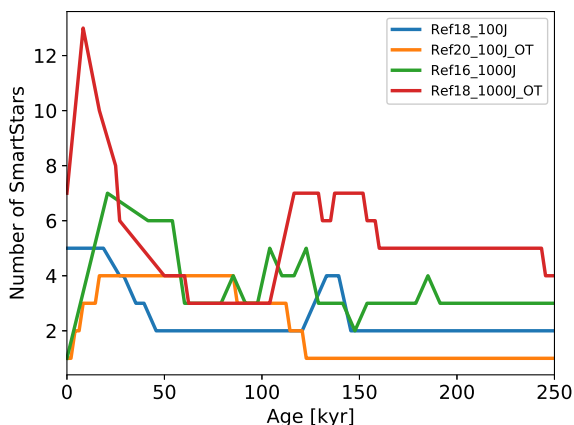


**Figure 3.** The number of *SmartStars* as a function of time for the highest resolution runs for the case of the 100  $J_{21}$  and 1000  $J_{21}$  backgrounds. In both cases the level of fragmentation peaks at the start and due to mergers and accretion saturates after less than 200 kyr. The number of *SmartStars* is systematically higher for the higher background due to the fact that the central gas core, out of which the *SmartStars* form is larger for the higher background.

the results of a simulation run a refinement level of 16 but with full radiative transfer for comparison. The blue line, representing the accretion history of the *SmartStar* for the 1  $J_{21}$  background has the lowest accretion rates and the accretion rate quickly drops below the critical threshold (dashed horizontal line) - this particle switches type to a Pop III star as expected for a low background. For the 100  $J_{21}$  (green line) the accretion history shows that the star initially fluctuates between being a SMS and being a Pop III star for approximately the first 80 kyr of its lifetime after which the

accretion rate recedes below the critical threshold and while there are subsequent increases in the accretion rate, the rate never again exceeds the critical level. The red line and the cyan line are the accretion histories for the 1000  $J_{21}$  background. The difference in the two cases is that for the red line the full radiative transfer is used but the refinement level is reduced by a factor of four. For the maximum refinement case the radiation is modelled in the optically thin mode with only non-ionising radiation included. Nonetheless, the agreement is remarkable. The high accretion rates mean that the star is always of type SMS and so the radiation is confined to the non-ionising regime. Even more satisfying is the convergence between the simulations. The slightly lower resolution run (red line) gives broadly the same accretion history as the higher resolution run (cyan line).

In the right hand panel of Figure 1 we plot the total mass accreted by the largest particle in each simulation. We also overplot the total stellar mass accreted by all particles in each simulation (dashed lines). Starting with the 1  $J_{21}$  background we see that the accretion rates lead to a total mass of a few hundred  $M_{\odot}$  after 250 kyr at which point the accretion rates have dropped significantly and this will be close to the final mass. While this mass is clearly above the characteristic mass found by other authors (Turk et al. 2009; Stacy et al. 2010; Clark et al. 2011; Stacy et al. 2012) our resolution is too low to resolve fragmentation in these Pop III systems and the mass ascribed here should be taken as a reasonable upper limit. For the Ref18\_100J simulation (green line), the mass of the largest *SmartStar* is closer to  $10^4 M_{\odot}$  while for the 1000  $J_{21}$  the mass has increased by an order of magnitude up to  $10^5 M_{\odot}$ . The difference between the red and cyan line in this case again emphasises the excellent convergence that is achieved with a difference in the final mass (after 250 kyr) of less than a factor of 2.

In Figure 2 we again test for convergence in our spatial resolution using the 100  $J_{21}$  background simulations only. We look at the difference between maximum spatial resolutions that range

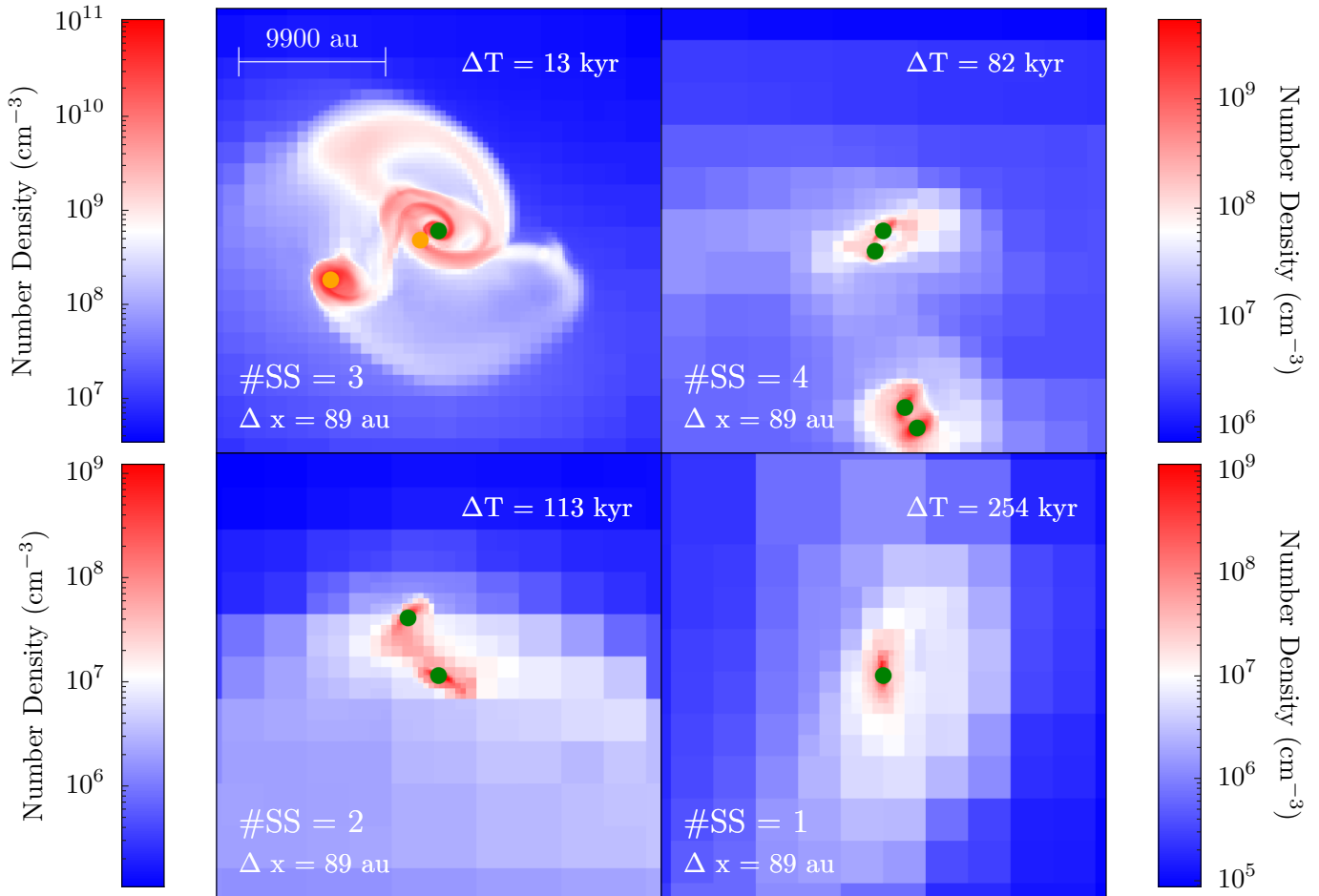


**Figure 4.** A projection along the “y” axis of the box centred on the most massive *SmartStar* in each panel. The depth of each projection is 30000 AU and is density weighted. Shown is the evolution of the clumps within the collapsing halo for the Ref20\_100J\_OT simulation. Green circles indicate Pop III stars while orange circles indicate SMSs. Initially two clumps form at the centre of the collapsing structure. The gas continues to fragment forming two separate binary systems. The double binary evolves before the individual clumps within the binary merge - the first after 80 kyr and the second subsequently after 110 kyr. The binary, that is left, quickly merges then to form a single Pop III star at the centre of the halo with no further fragmentation observed up to 250 kyr. No three body interactions occur in this simulation.

from 10 levels of refinement up to 20 levels of refinement (corresponding to  $\sim 10000$  AU down to  $\sim 90$  AU). The very high resolution Ref20 simulation uses the optically thin approximation for the non-ionising radiation and neglects ionising photons. The blue line, represents the accretion history of the Ref10 simulation and has the highest accretion rate over the course of the first 250 kyr and exceeds the critical rate. The accretion rate then drops below the critical rate for the remainder of the lifetime of the star. Both the Ref14, Ref18 and the very high resolution Ref20 simulations show lower accretion rates. The Ref18 and Ref20 simulations show more variation compared to the Ref14 simulation due to the increased resolution and therefore the ability of the hydro solver to identify smaller clumps of material which may then subsequently be accreted by the central core. However, the degree of convergence between the Ref20 (cyan) and Ref18 (red) lines is again quite remarkable. There is more initial fragmentation in the Ref18 simulation and then those fragments (stars) merge (this is the main reason behind the spikes in accretion seen at 45 and 70 kyr).

In the right hand panel of Figure 2 we show the total stel-

lar mass for both the largest *SmartStar* and for the total mass from all the *SmartStars* formed. The lowest resolution, blue line, clearly overestimates the accretion rate and hence the final mass and this has been shown before to be a problem for low resolution simulations (e.g. [Negri & Volonteri 2017](#)). The maximum resolution for the Ref10 run is approximately 0.44 pc, the bondi radius of a star with a mass of  $1000 M_{\odot}$  in an atomic cooling halo is of the order of 0.5 pc. Given the Ref10 simulation is not able to resolve the Bondi radius around the accreting star even once it’s mass reaches  $1000 M_{\odot}$  it is not surprising that the mass is overestimated. Only once the refinement is sufficient to resolve the bondi radius do we begin to see convergence. After 250 kyr the difference in total stellar mass between the Ref14, Ref18 and Ref20 runs is less than a factor of 2. The total stellar mass converges towards a mass of approximately  $10^4 M_{\odot}$  after 250 kyr. However, the largest portion of the growth of the *SmartStars* takes place within the first 100000 years. The sharp spikes seen in the Ref18 and Ref20 runs indicate the somewhat chaotic nature of the accretion. No fragmentation (see below) is seen for the Ref14 simulation (hence no

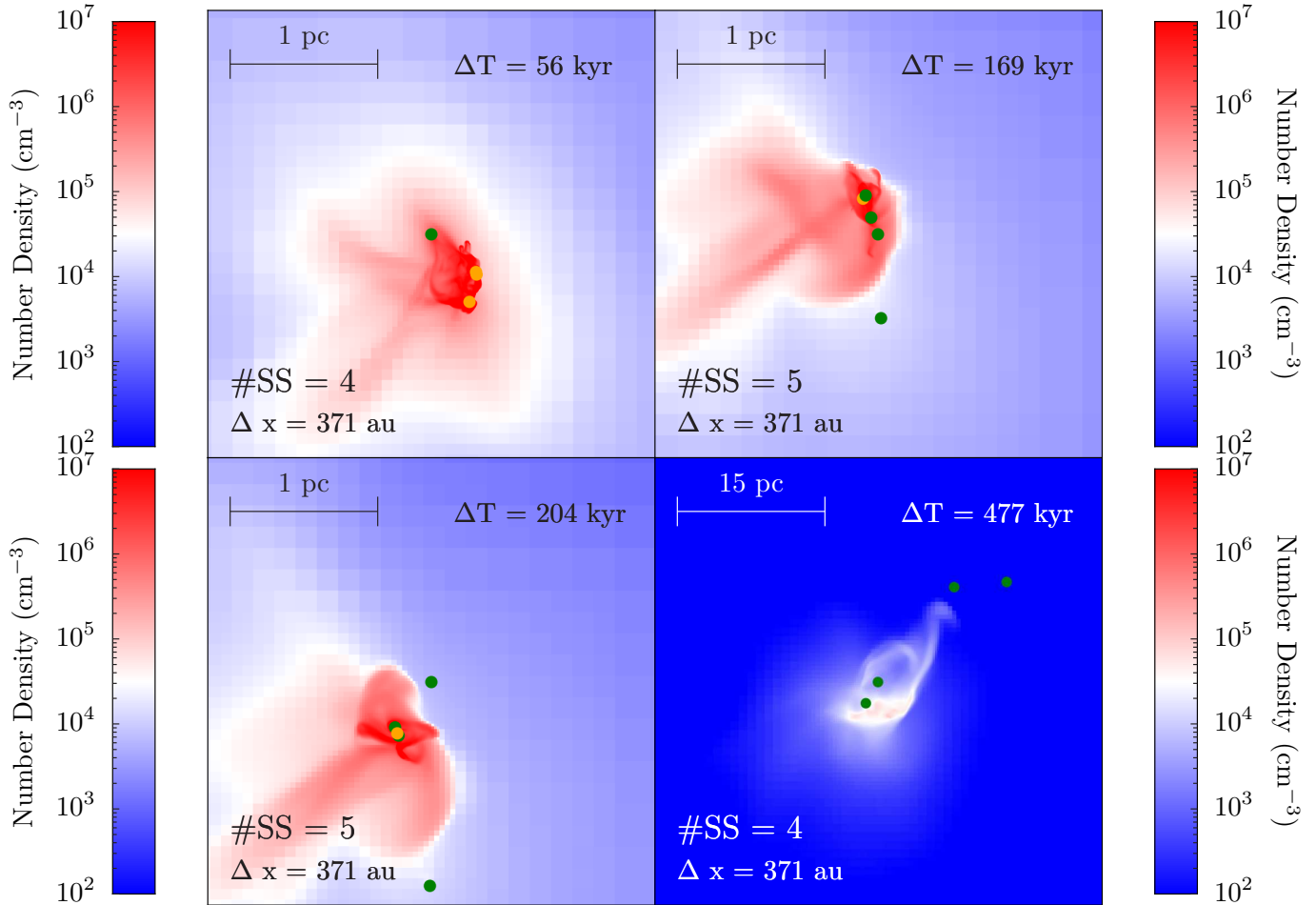


**Figure 5.** We show visualisations of the Ref18\_1000J\_OT simulation for four different times extending up to nearly 500 kyr after the formation of the first SmartStar. The visualisations are centred on one of the least massive SmartStars which always sits near the centre of the potential. We do this to illustrate the ejection of two of the most massive SmartStars from the centre. Within the 1000  $J_{21}$  simulation 4 SmartStars exist after 56 kyr. As the simulation progresses one additional SmartStar forms and then merges again with the central most massive SMS. Between 100 kyr and 200 kyr several multiple body interactions combined with the depleted central gas densities cause the two most massive SmartStars to become ejected (see bottom right panel). After approximately 450 kyr (bottom right panel) the high density gas has been removed by the accreting stars. SMSs are colour coded orange and Pop III stars are coloured green.

dashed line) while multiple fragments (stars) are found for both the Ref18 and Ref20 simulations. We will now examine the fragmentation in our simulations in more detail.

### 3.2 Fragmentation within the star forming galaxy

In Figure 2 neither the Ref10 or the Ref14 runs show any signatures of fragmentation. In both cases only a single central star forms. However, as we increase the resolution we are able to better capture fragmentation, especially for the 1000  $J_{21}$  backgrounds where the accretion rates and hence masses of the stars are larger. In Figure 3 we plot the number of SmartStars as a function of time. Time equal to zero corresponds to the formation of the first SmartStar in the simulation. We plot the evolution of the two highest resolution runs in the 100  $J_{21}$  and 1000  $J_{21}$  cases. In all cases there is initially a spike in fragmentation - most pronounced in the 1000  $J_{21}$  due to the more massive halo under going collapse. In the case of the Ref18\_100J simulation five SmartStars form

within 7 kyr of the first SmartStar in a small clustered region with an average separation of approximately 2500 AU between the SmartStars. Similarly, the Ref18\_1000J undergoes initial vigorous fragmentation with seven SmartStars forming within 5.5 kyr of each other again in a clustered region with an average separation again of approximately 2500 AU. Recall, that the merger and accretion radii of the SmartStars in the Ref18 simulations is four cell widths corresponding to approximately 1500 AU. The stars are therefore forming just outside the merger radius of the stars. As a result in all cases the SmartStars tend to merge and the system reaches an equilibrium after almost 150 kyr. The 100  $J_{21}$  case is especially interesting. After 50 kyr the Ref20 run has 4 SmartStars while the lower resolution Ref18 run has two SmartStars. Upon closer inspection (see Figure 4) we see that the Ref20 system is made up of two separate binaries. The Ref18 run was simply unable to resolve the fragmentation of the separate systems into binaries. Similarly, the 1000  $J_{21}$  simulations show that the higher resolution systems are able to resolve more fragments.



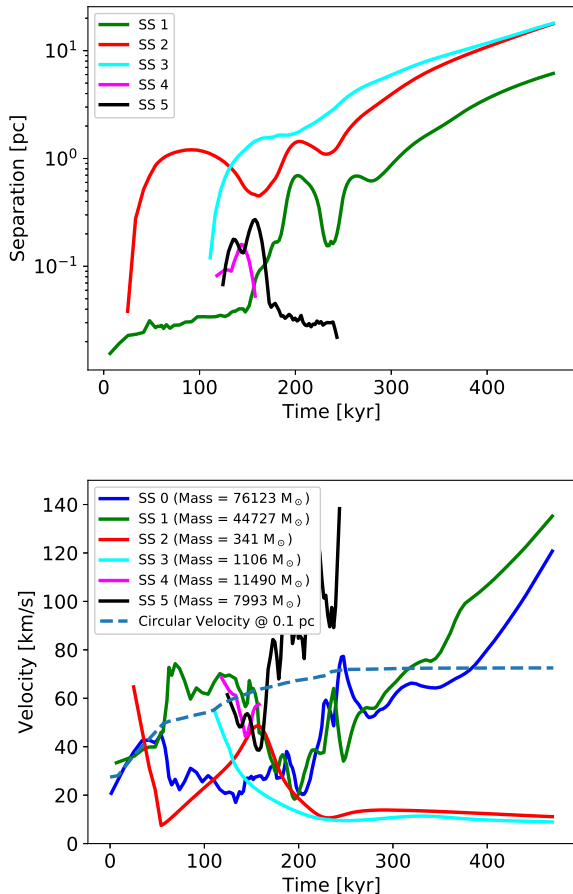


**Figure 6.** The evolution of the separations between each SmartStar and the most massive SmartStar and the velocities of all of the SmartStars in the Ref18\_1000J\_OT simulation. Only SmartStars which survive for more than 10 kyr are plotted. *Upper Panel:* The separation between the most massive SmartStar, SS 0, and the other SmartStars. All of the SmartStars are born, with the possible exception of SS 3, within 0.1 pc of the most massive SmartStar. As the system develops and multiple three body interactions occur SS 0 and SS 1 are ejected from the halo centre. SS 4 and SS 5 are involved in mergers at 150 kyr and 250 kyr respectively. *Bottom Panel:* The evolution of the velocities of the SmartStars. The circular velocity of the halo within 0.1 pc of the centre of the halo is also shown. Several multi-body interactions between 100 kyr and 200 kyr result in the ejection of SS 0 and SS 1 (their masses are  $76123 M_{\odot}$  and  $44727 M_{\odot}$  respectively). Two lower mass SmartStars are left at the centre of the halo with low velocities.

In Figure 4 we show visualisations at 4 different epochs showing the emergence of fragments (stars) during the evolution of the simulation with a background of 100  $J_{21}$  and at the maximum refinement level. The projection is aligned along the “y” axis of the simulation centred on the most massive SmartStar in each panel. The depth of each projection is 30000 AU and is density weighted. In the top left panel the simulation axis is fortuitously aligned with the spiral arms of the accretion disk. Any accretion disk is however short-lived as the motions of both the gas and the SmartStars destroy any coherent disks and deplete the gas reservoir. In the top left panel we show the initial state of the system 7 kyr after the formation of the first SmartStar particle. At this stage two particles have formed. As the system evolves another binary system develops at a separation of approximately 10000 AU.

The two binary systems remain stable through out the first 100 kyr of their existence before merging (at which point the simulation results converges to the lower resolution Ref18 results). We now examine more closely the double binary system and the evolution of the system.

### 3.3 Binary Systems and Stellar Ejections

We select the pair of binary systems that form in the highest resolution simulation with the 100  $J_{21}$  background. The system is visualised in Figure 4, the stars are colour coded with SMSs coloured orange and Pop III stars coloured green. All four stars contract to the main sequence and form massive Pop III stars as the systems evolve. Note that for this very high resolution run we had to switch off ray tracing and so we do not follow the ionising radiation. By the time the oldest Pop III star is approximately 250 kyr old it has a mass of almost  $10^4 M_{\odot}$ . The separations of both binary systems vary between 1000 AU and 3000 AU over the course of almost 100 kyr. After approximately 80 kyr the first binary system coalesces with the second binary coalescing shortly afterwards. This results in the formation of a “new” binary with an initial separation of approximately 10000 AU. This new binary coalesces after a further 10 kyr leaving a single SmartStar with a mass of  $\sim 15000 M_{\odot}$ . The single SmartStar continues to accrete mass at a rate of  $\dot{M} \sim 10^{-2} M_{\odot}/\text{yr}$  at the centre of the potential.

The 1000  $J_{21}$  background simulations have a larger number of SmartStars and form a more diverse system with no tight binaries forming. Due to the very high initial accretion rates (see Figure 1) the mass of the largest SmartStar increases rapidly and after 250 kyr has a mass of almost  $10^5 M_{\odot}$ . In Figure 5 we show the evolution of that system at four different times. The number of SmartStars varies between 4 and 5 during the course of the evolution. A series of close encounters between the SmartStars occurring between 100 kyr and 200 kyr results in the ejection of two of the most massive SmartStars from the centre of the halo with velocities which exceed the escape velocity of the core of the halo. In Figure 6 we plot the separation (upper panel) of each SmartStar from the most massive SmartStar and the individual particle velocities (bottom panel) as a function of time. The circular velocity for the halo at a radius of 0.1 pc ( $\sim 20000\text{AU}$ ) is also plotted. SS 0 is not plotted in the upper panel of Figure 6 because the separations are relative to SS 0. SS 1, SS 3, SS 4 & SS 5 are all in close proximity to SS 0 at around the 100 kyr mark. Between 100 kyr and 250 kyr the particles all undergo complex dynamical interactions which lead to mergers and kicks to the particles eventually leading SS 0 to be ejected from the halo. In the bottom panel of Figure 6 we plot the velocities of the particles. The close encounters and mergers (for example star SS 5 merges with SS 0 after 230 kyr) results in sharp increase to the velocities to a number of the stars. These kicks are sufficient to eject the two most massive stars from the centre of the halo with velocities of more than  $100 \text{ km s}^{-1}$ . While the ejected stars initially receive large accelerations the accelerations quickly dissipate but the velocities and trajectories at this point are more than sufficient to escape the halo. The two least massive stars which are left in the centre have small velocities of approximately  $10 \text{ km s}^{-1}$  but low accretion rates as they are essentially starved by their more massive siblings. Upon being ejected from the halo the two most massive stars carry more than  $10^5 M_{\odot}$  of gas out of the halo dramatically altering the gravitational potential of the halo centre.

The most massive stars exit the central region and their accretion rates decline significantly (see §3.5). It should be noted at this

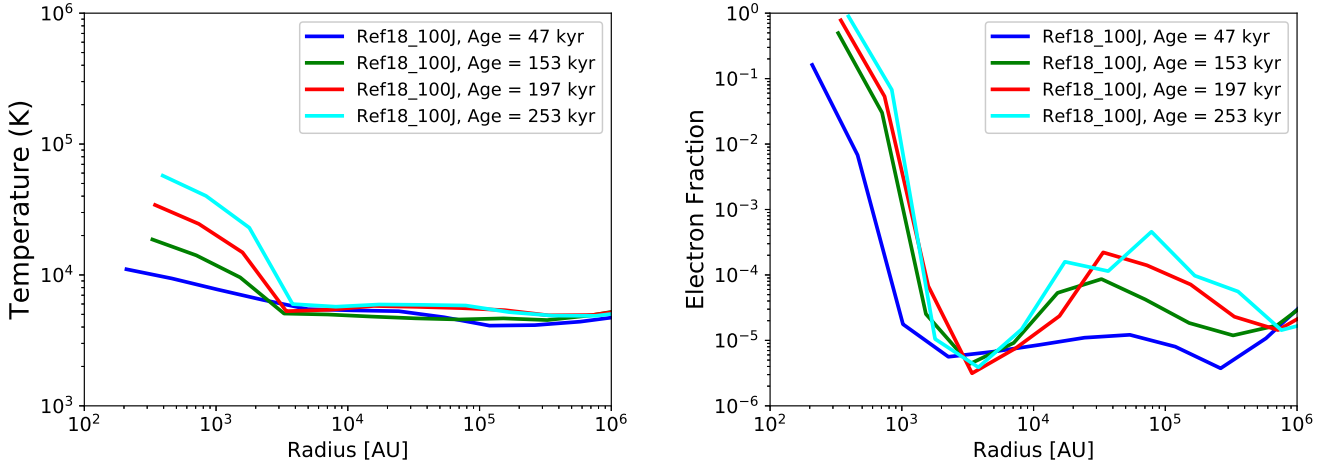


**Figure 7.** Radial profiles of the Ref18\_100J simulation for 4 different times. The star initially fluctuates between being a SMS and a Pop III before the accretion rate drops and the star contracts to the main sequence. After 50 kyr the star is always in the Pop III cycle. In the left hand panel we show the temperature profile and in the right hand panel the electron fraction. All profiles are centred on the most massive star in the simulation. The maximum resolution of the Ref18 simulation is approximately 200 AU. The high gas density surrounding the star means that radiative cooling is still very effective at regulating the temperature as well as containing the HII region. The electron fraction, while very high close to the star, drops sharply only a few cells from the star.

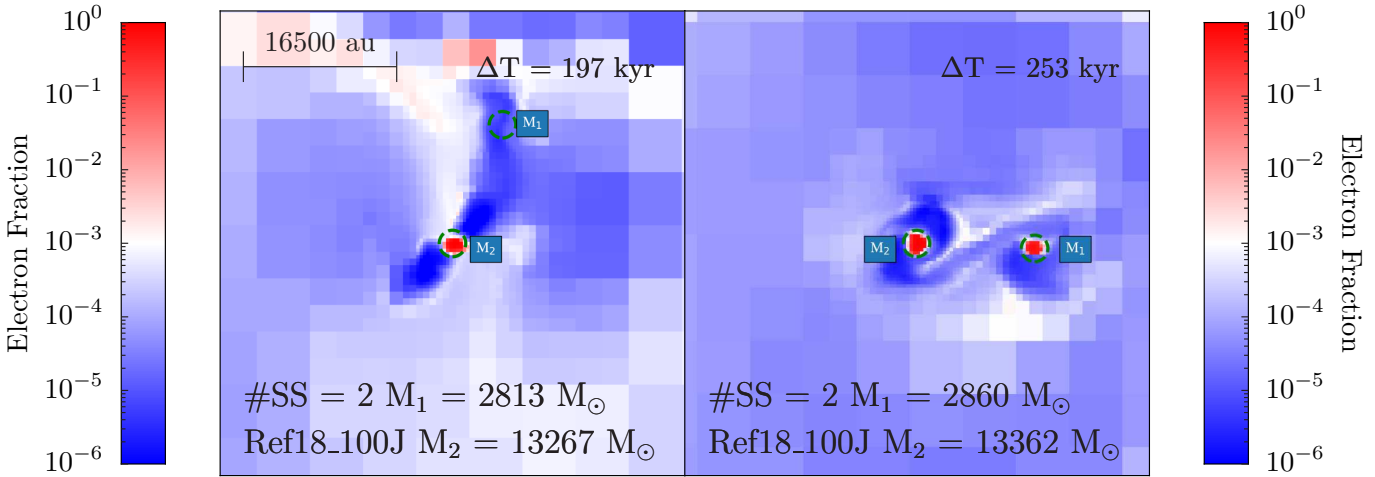


**Figure 8.** Slices of the Electron Fraction for the last two output times shown in Figure 7. The dashed green lines identify the Pop III in each case and are set to the radius of the accretion sphere. The electron fraction observed around the central, most massive star indicates the extent of the HII region and that it is confined to a volume close to the star.

point that the stellar mass at the centre dominates the gravitational potential relatively quickly after formation due to their very high accretion rates. Hence, the stars are very unstable to ejections because there is little high density gas left to provide a gravitational attraction. These ejected stars are hyper-velocity stars with enough velocity to exit the halo (the escape velocity of the halo is only  $20 \text{ km s}^{-1}$ ). These massive stars, final masses of  $76123 M_{\odot}$  and  $44727 M_{\odot}$  respectively, will form a population of wandering massive black holes (e.g. [Tremmel et al. 2018](#)).

We select a merger radius for all stars in our simulations at 4 cell widths. Therefore, mergers and close encounters occur at the edge of our resolution. The gravity solver in Enzo is a particle mesh

gravity solver with an effective resolution of twice the cell spacing - therefore our gravitational resolution is two cell spacings. Increasing our merger radius may eliminate these ejections by dulling our ability to capture fragmentation. By setting our merging radius at this low value we are marginally able to track these stars at the cost that these close encounters, and their resulting kicks, are only marginally resolved. As we simulate only a single halo, albeit at varying resolution and with different external backgrounds, our results can not be ascribed to all haloes. Our results are qualitative in that ejections likely play a role when multiple massive fragments form in close proximity but placing quantitative values on the fraction of haloes which experience ejections or on the exact

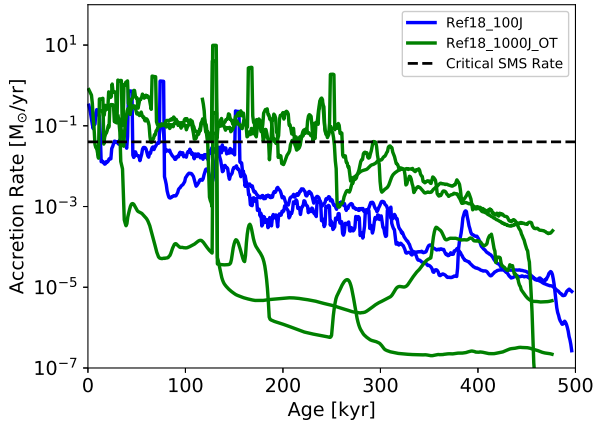


**Figure 9.** The mass accretion rate onto all the *SmartStars* which survive to the end of the Ref18\_100J and Ref18\_1000J\_OT simulations. The Ref18\_100J are coloured blue while the Ref18\_1000J\_OT simulations are coloured green. Two of the most massive particles are ejected from the Ref18\_1000J\_OT and they show a rapid decrease in accretion rates after the ejection (at  $\sim 200$  kyr). The other two *SmartStars* in the Ref18\_1000J\_OT have low accretion rates throughout. In the Ref18\_100J simulations multi-body interactions early in the evolution of the system (before 50 kyr) give large kicks to the remaining two particles causing them to be ejected from the central core of the halo and causing a decrease in their accretion rates.

environmental conditions which either promote or suppress ejections is outside the scope of this work.

### 3.4 Feedback from the Pop III stars

As the stars evolve their individual accretion rates determine whether they are able to sustain a bloated envelope and remain a SMS or whether they contract to the main sequence and become massive Pop III stars. In our subgrid implementation we set the critical threshold at  $0.04 M_{\odot}/\text{yr}$  and allow particles to remain as SMSs as long as any dips below this threshold are shorter than 1000 years (Sakurai et al. 2016). Nonetheless, for our fiducial 100  $J_{21}$  runs none of the particles that form are able to sustain accretion rates above  $0.04 M_{\odot}/\text{yr}$ . Even in the Ref10 runs (where as we noted low resolution results in artificially high accretion rates) the star transitions to a massive Pop III star rather than a SMS after approximately 300 kyr. For the Ref14 and Ref18 cases the accretion rates quickly fall below the critical threshold and the stars contract to the main sequence. As the stars contract to the main sequence the radiation feedback switches from an effective temperature of  $T_{\text{eff}} = 5000\text{K}$  to  $T_{\text{eff}} = 10^5\text{K}$ . The resulting radiation spectrum switches from predominantly infrared radiation to predominantly UV radiation. In Figure 7 we plot the temperature and electron fraction as a function of radial distance. In all cases the profiles are centred on the most massive Pop III star which emits a spectrum based on a blackbody temperature of  $T_{\text{eff}} = 10^5\text{K}$ . The temperature of gas is initially close to isothermal even up to the accretion radius of the Pop III star. The high gas densities surrounding the stars are effective in regulating the central temperatures at close to  $10^4\text{K}$ . As the ionising radiation from the Pop III star starts to ionise and heat the surrounding gas the temperature increases and has reached a value of around  $6 \times 10^4\text{K}$  after 250 kyr. The electron fraction (right hand panel of Figure 7) shows a sharp increase

in the electron fraction close to the star as the HII region expands and reaches a value of unity close to 1000 AU. However, the high gas column densities successfully shield the gas and prevent the HII region expanding much beyond that, with the electron fraction returning to values close to  $10^{-5}$  at 3000 AU. In Figure 8 we plot slices through the electron fraction field showing the impact of the ionising radiation from the last two snapshots shown in Figure 7. In both panels the electron fraction reaches values well above 0.1 within the accretion radius of each Pop III star with dense, neutral, gas sitting around the Pop III stars. The extent of the HII region is no more than a few cells wide - a few thousand AU at most. The high density of the surrounding gas, combined with the high infall rates limit the ability of the HII regions to expand.

Upon contraction to the main sequence the Pop III star radii fall well below our resolution limits. Given we set the accretion radius at 4 cells in radius we are therefore most likely over estimating the accretion onto the Pop III star as the ability of the gas to discard angular momentum at scales near the star can clearly not be captured by this work. The feedback scheme implemented here scales with the mass of the star - we are therefore also over estimating the feedback intensity from the stars. Even in over estimating the feedback it is nevertheless trapped close to the star and hence our conclusion that feedback from Pop III stars in regions of high infall does not negatively effect the infall is robust.

We also note that the results found for the Pop III stars are consistent with those for present day massive star formation. Results from simulations of present day massive star formation (e.g. Peters et al. 2010; Krumholz 2015) show that fragmentation is less of an issue than was once believed. Similar to the results found here many authors (within the present day star formation community) have found that radiative feedback is successful at heating the gas thus suppressing fragmentation. Ionising radiation which can drive large HII regions has also been found to be unable to halt the accretion flow as long as the flow is maintained and the HII regions' expansion subdued (Walmsley 1995; Peters et al. 2011).

### 3.5 Towards forming a massive black hole seed

Due to the high computational cost we are unable to evolve our highest resolution simulations, even when running in optically thin mode, much beyond 250 kyr within a reasonable timeframe. Nonetheless, for some of the lower resolution runs we can explore the future fate of these objects. As can be concluded from Figures 1 and 2 after approximately 100 kyr the total mass of the *SmartStars* saturates and the accretion rate also saturates. Furthermore, our examination of the stellar dynamics at the centre of the potential when multiple interactions occur show that massive bodies can be flung out from the centre of the halo thus severely diminishing their accretion rates. This result is borne out in Figure 9 where we plot the accretion rate up to 500 kyr after the formation of the first *SmartStar* for all of the stars which survive to the end of the Ref18\_100J and Ref18\_1000J\_OT simulations. Each of the stars trace a unique accretion history. The two most massive stars in the Ref18\_1000J\_OT simulation have high accretion rates until approximately 250 kyr after their formation. At this point, as already discussed in §3.3, the stars get ejected from the central core and their accretion rates drop dramatically. The Ref18\_100J simulation exhibits a similar event, a four body interaction at 140 kyr causes the ejection of the two surviving *SmartStars* from the system and with it a significant drop in accretion as the *SmartStars* leave the high density region. Therefore, while both the Ref18\_100J and Ref18\_1000J\_OT simulations form

massive Pop III stars, after approximately 500 kyr the stars also get ejected due to multi-body interaction. These stars will leave the halo, collapse into black holes but be unable to grow.

In our highest resolution run, Ref20\_100J, there were fewer multibody interactions. In this system a single massive Pop III star remains at the centre of the rapid inflow after 250 kyr. While the prohibitive computational cost of this high resolution system leaves us unable to evolve this system for more than 250 kyr, at this evolutionary stage this single surviving Pop III star is likely to remain at the centre of the potential accreting at relatively high accretion rates ( $\dot{M} \sim 10^{-2} M_{\odot}/\text{yr}$ ) and ending its life with a mass of approximately  $2 \times 10^4 M_{\odot}$ . This Pop III star will then directly collapse into a black hole of the same mass continuing to accrete mass. If the accretion rate at this time remains at levels close to  $\dot{M} \sim 10^{-2} M_{\odot}/\text{yr}$  this value will exceed the canonical Eddington rate by a factor of close to 100. Feedback from the black hole will likely quickly regulate the accretion rate. Nonetheless, the black hole will be centred at the apex of the gravitational potential supported by a high inflow rate and therefore likely to experience high or super critical accretion rates. Therefore, for the case of the 100 J<sub>21</sub> at the highest resolution we find that conditions, for this halo, are optimal for forming a rapidly accreting black hole seed.

#### 4 SUMMARY & DISCUSSION

In this study we have tracked the formation of SMSs and massive Pop III stars in haloes experiencing high inflow of up to  $1 M_{\odot}/\text{yr}$ . We have used two different LW backgrounds of 100 J<sub>21</sub> and 1000 J<sub>21</sub> to create the necessary environmental conditions. We find that with a background of 100 J<sub>21</sub> a massive Pop III star forms. The most massive star to form under such a background initially experiences sufficient accretion rates to allow its envelope to expand and it forms a SMS, however, the star cannot maintain the required accretion rates and after less than 100 kyr contracts to the main sequence. The 1000 J<sub>21</sub> is able to induce a critical accretion rate for at least 250 kyr and a SMS forms. Under both backgrounds mild fragmentation is observed within the collapsing gas. The birth of multiple fragments within the tight confines leads to tight binaries and subsequent coalescences but also to violent, multibody, dynamical interactions leading to the ejections of stars in many cases. In our highest resolution simulation with a background of 1000 J<sub>21</sub> a series of close encounters results in the ejection of the two SMSs from the centre of the halo. The ejection results in hugely diminished accretion rates and the stars contract to the main sequence on their way out of the halo. In the highest resolution simulation with a background of 100 J<sub>21</sub> multiple interactions between multiple stars are fortuitously avoided (due to mergers) and the systems settle with one massive Pop III star accreting at the centre of the halo.

The very high inflow rates suppress the impact of the ionising radiation from the massive Pop III stars which form. HII regions do form around the Pop III stars but surrounding high density gas effectively absorbs the emitted radiation arresting the propagation of the HII region much beyond a few cell widths from the Pop III stars. Our maximum resolution is of the order of 100 AU and so while this is marginally sufficient to capture SMS formation and the accretion onto the outer envelope of a SMS it is insufficient to follow the accretion onto the surface of a Pop III as it contracts on the Kelvin-Helmholtz timescale. In our scheme we assume that gas that is flowing radially inward at close to our maximum resolution makes it onto the surface of the star. There are clearly inherent limi-

tations to this approach and we are likely over estimating the accretion rate onto Pop III stars. Nonetheless, we observe that feedback from these, very massive, Pop III stars is unable to evacuate a significant HII region due to the high mass inflow and we conclude that this is a robust result from our simulations. A further caveat of our simulation setup is the imposition of a LW background. The background is necessary to suppress H<sub>2</sub> formation and allow for the formation of atomic cooling haloes with sufficient inflow rates to investigate the formation of a SMS. However, the environment is somewhat artificial as the nearby star forming galaxies which would in reality create the LW radiation are absent along with their gravitational impact on the simulated galaxy. These nearby galaxies may induce torques which could potentially suppress or enhance the accretion rates and also facilitate future mergers. We will investigate more, cosmologically realistic, environments in an upcoming study.

Chon et al. (2018) undertook a recent study where they explored the formation of SMSs drawn from realistic cosmological simulations, albeit also with the imposition of an artificial LW background to suppress H<sub>2</sub>. Chon et al. (2018) investigated two collapsing haloes - one which was subject to significant dynamical torques (filamentary collapse) and one where the tidal field was relatively weak (spherical collapse). In both cases they follow the evolution of the SMSs for 100 kyr at very high resolution. Similar, to our findings they report the formation of SMSs with accretion rates exceeding the critical rate. They find that mild fragmentation is also prevalent in their simulations with more than 10 stars forming in their filamentary galaxy. In their simulations the primary protostar maintains a super-critical accretion rate for the majority of the 100 kyr. They do not see any ejections of stars from their galaxy in the first 100 kyr. However, this timescale is relatively short - representing only approximately 10% of the lifetime of the most massive primary star. Ejections in our simulations only became evident after approximately 200 kyr as the interactions of the stars take time to develop with the system undergoing significant evolution in the first 200 kyr with new stars forming and mergers common. Nonetheless, the two sets of simulations are broadly consistent with protostars showing super-critical accretion rates and the formation of multiple stars in both cases.

Our simulations show that the formation of both massive Pop III stars and SMSs is viable in regions of high accretion. Feedback in both cases has little or no negative impact on the accretion flow at the scales probed in our work. Addressing the future fate of these objects is less trivial. As discussed above the SMSs which form and evolve with rates above the critical limit in the 1000 J<sub>21</sub> simulations both experience violent dynamical interactions which result in their expulsion from the halo. While these seeds will likely go on to form massive seed black holes they will be far from the halo centre and likely unable to accrete any further gas. In the 100 J<sub>21</sub> case a single Pop III star forms at the centre of the collapse and while its accretion rate is sub-critical for SMS expansion the very high accretion rates would be significantly super-Eddington for a black hole of comparable mass. If this massive Pop III star directly collapses to a black hole and remains at the centre of a strong accretion flow the conditions are very favourable for achieving super critical accretion if the angular momentum of the gas can be shed efficiently (Begelman & Volonteri 2017; Sugimura et al. 2018). It could also be that magnetic fields induced by the initially magnetised gas and amplified by the small scale dynamo effect (Schleicher et al. 2010; Sur et al. 2010; Turk et al. 2012; Schober et al. 2012, 2013) induce angular momentum transport helping to maintain very high accretion rates.

Finally, the lighter levels of fragmentation in the 100  $J_{21}$  are a further attraction as this leads to a lower probability of ejection from the halo something that may effect larger systems which may suffer higher levels of fragmentation. A more thorough exploration of the formation of massive seeds will require a more realistic treatment of the dynamical environment in which the conditions for massive star formation becomes possible.

## ACKNOWLEDGEMENTS

J.A.R. acknowledges the support of the EU Commission through the Marie Skłodowska-Curie Grant - “SMARTSTARS” - grant number 699941. Computations described in this work were performed using the publicly-available `Enzo` code (<http://enzo-project.org>), which is the product of a collaborative effort of many independent scientists from numerous institutions around the world. Their commitment to open science has helped make this work possible. The freely available astrophysical analysis code `YT` (Turk et al. 2011) was used to construct numerous plots within this paper. The authors would like to extend their gratitude to Matt Turk et al. for an excellent software package. J.A.R. would like to thank Lydia Heck and all of the support staff involved with Durham’s COSMA4 and DiRAC’s COSMA5 systems for their technical support. This work was supported by the Science and Technology Facilities Council (grant numbers ST/L00075X/1 and RF040365). This work used the DiRAC Data Centric system at Durham University, operated by the Institute for Computational Cosmology on behalf of the STFC DiRAC HPC Facility ([www.dirac.ac.uk](http://www.dirac.ac.uk)). This equipment was funded by BIS National E-infrastructure capital grant ST/K00042X/1, STFC capital grant ST/H008519/1, and STFC DiRAC Operations grant ST/K003267/1 and Durham University. DiRAC is part of the National E-Infrastructure. The authors also wish to acknowledge the SFI/HEA Irish Centre for High-End Computing (ICHEC) for the provision of computational facilities and support. Furthermore, the authors would like to thank John Wise and Marta Volonteri for useful discussions and comments on earlier manuscript drafts. Finally, the authors would like to thank the referee for a constructive report.

## REFERENCES

- Agarwal B., Khochfar S., 2015, *MNRAS*, 446, 160
- Agarwal B., Khochfar S., Johnson J. L., Neistein E., Dalla Vecchia C., Livio M., 2012, *MNRAS*, 425, 2854
- Agarwal B., Davis A. J., Khochfar S., Natarajan P., Dunlop J. S., 2013, *MNRAS*, 432, 3438
- Agarwal B., Dalla Vecchia C., Johnson J. L., Khochfar S., Paardekooper J. P., 2014, *MNRAS*, 443, 648
- Ahn K., Shapiro P. R., Iliev I. T., Mellema G., Pen U. L., 2009, *ApJ*, 695, 1430
- Alvarez M. A., Wise J. H., Abel T., 2009, *ApJ*, 701, L133
- Bañados E. et al., 2017, *ArXiv e-prints*
- Begelman M. C., Volonteri M., 2017, *MNRAS*, 464, 1102
- Begelman M. C., Volonteri M., Rees M. J., 2006, *MNRAS*, 370, 289
- Berger M. J., Olinger J., 1984, *Journal of Computational Physics*, 53, 484
- Boekholt T. C. N., Schleicher D. R. G., Fellhauer M., Klessen R. S., Reinoso B., Stutz A. M., Haemmerl L., 2018, *MNRAS*, 476, 366
- Bryan G. L., Norman M. L., Stone J. M., Cen R., Ostriker J. P., 1995, *Computer Physics Communications*, 89, 149
- Bryan G. L., Norman M. L., O’Shea B. W., Abel T., Wise J. H., Turk M. J., The Enzo Collaboration, 2014, *ApJS*, 211, 19
- Chon S., Hosokawa T., Yoshida N., 2018, *MNRAS*
- Clark P. C., Glover S. C. O., Smith R. J., Greif T. H., Klessen R. S., Bromm V., 2011, *Science*, 331, 1040
- Coppola C. M., Longo S., Capitelli M., Palla F., Galli D., 2011, *ApJS*, 193, 7
- Coppola C. M., D’Introno R., Galli D., Tennyson J., Longo S., 2012, *ApJS*, 199, 16
- Dijkstra M., Haiman Z., Mesinger A., Wyithe J. S. B., 2008, *MNRAS*, 391, 1961
- Dijkstra M., Ferrara A., Mesinger A., 2014, *MNRAS*, 442, 2036
- Federrath C., Banerjee R., Clark P. C., Klessen R. S., 2010, *ApJ*, 713, 269
- Glover S. C. O., 2015a, *MNRAS*, 451, 2082
- Glover S. C. O., 2015b, *MNRAS*, 453, 2901
- Glover S. C. O., Abel T., 2008, *MNRAS*, 388, 1627
- Glover S. C. O., Jappsen A. K., 2007, *ApJ*, 666, 1
- Glover S. C. O., Savin D. W., 2009, *MNRAS*, 393, 911
- Haemmerl L., Woods T. E., Klessen R. S., Heger A., Whalen D. J., 2017, *ArXiv e-prints*
- Haemmerl L., Woods T. E., Klessen R. S., Heger A., Whalen D. J., 2018, *MNRAS*, 474, 2757
- Hahn O., Abel T., 2011, *MNRAS*, 415, 2101
- Haiman Z., 2006, *New Astronomy Review*, 50, 672
- Hirano S., Hosokawa T., Yoshida N., Umeda H., Omukai K., Chiaki G., Yorke H. W., 2014, *ApJ*, 781, 60
- Hirano S., Hosokawa T., Yoshida N., Kuiper R., 2017, *Science*, 357, 1375
- Hockney R. W., Eastwood J. W., 1988, *Computer simulation using particles*. Bristol: Hilger, 1988
- Hosokawa T., Yorke H. W., Omukai K., 2010, *ApJ*, 721, 478
- Hosokawa T., Omukai K., Yoshida N., Yorke H. W., 2011, *Science*, 334, 1250
- Hosokawa T., Omukai K., Yorke H. W., 2013a, *ApJ*, 778, 178
- Hosokawa T., Yorke H. W., Inayoshi K., Omukai K., Yoshida N., 2013b, *ApJ*, 778, 178
- Hosokawa T., Hirano S., Kuiper R., Yorke H. W., Omukai K., Yoshida N., 2016, *ApJ*, 824, 119
- Inayoshi K., Tanaka T. L., 2015, *MNRAS*, 450, 4350
- Jeon M., Pawlik A. H., Bromm V., Milosavljević M., 2014, *MNRAS*, 440, 3778
- Johnson J. L., Khochfar S., Greif T. H., Durier F., 2011, *MNRAS*, 410, 919
- Katz H., Sijacki D., Haehnelt M. G., 2015, *MNRAS*, 451, 2352
- Kitsionas S., Whitworth A. P., 2002, *MNRAS*, 330, 129
- Krumholz M. R., 2015, in *Very Massive Stars in the Local Universe*, Astrophysics and Space Science Library, Volume 412. ISBN 978-3-319-09595-0. Springer International Publishing Switzerland, 2015, p. 43. Vol. 412, p. 43
- Krumholz M. R., McKee C. F., Klein R. I., 2004, *ApJ*, 611, 399
- Latif M. A., Volonteri M., 2015, *MNRAS*, 452, 1026
- Latif M. A., Bovino S., Grassi T., Schleicher D. R. G., Spaans M., 2015, *MNRAS*, 446, 3163
- Latif M. A., Schleicher D. R. G., Hartwig T., 2016, *MNRAS*, 458, 233
- Milosavljević M., Couch S. M., Bromm V., 2009, *ApJ*, 696, L146
- Mirocha J., Skory S., Burns J. O., Wise J. H., 2012, *ApJ*, 756, 94
- Mortlock D. J. et al., 2011, *Nature*, 474, 616
- Negri A., Volonteri M., 2017, *MNRAS*, 467, 3475

- O'Shea B. W., Norman M. L., 2007, *ApJ*, 654, 66
- Peters T., Klessen R. S., Mac Low M. M., Banerjee R., 2010, *ApJ*, 725, 134
- Peters T., Banerjee R., Klessen R. S., Mac Low M. M., 2011, *ApJ*, 729
- Planck Collaboration et al., 2014, *A&A*, 571, A16
- Regan J. A., Haehnelt M. G., 2009a, *MNRAS*, 396, 343
- Regan J. A., Haehnelt M. G., 2009b, *MNRAS*, 393, 858
- Regan J. A., Johansson P. H., Wise J. H., 2015, *MNRAS*, 449, 3766
- Regan J. A., Visbal E., Wise J. H., Haiman Z., Johansson P. H., Bryan G. L., 2017, *Nature Astronomy*, 1, 0075
- Reinoso B., Schleicher D. R. G., Fellhauer M., Klessen R. S., Boekholt T. C. N., 2018, *ArXiv e-prints*:1801.05891
- Sakurai Y., Vorobyov E. I., Hosokawa T., Yoshida N., Omukai K., Yorke H. W., 2016, *MNRAS*, 459, 1137
- Schaerer D., 2002, *A&A*, 382, 28
- Schauer A. T. P., Regan J., Glover S. C. O., Klessen R. S., 2017, *MNRAS*, 471, 4878
- Schleicher D. R. G., Banerjee R., Sur S., Arshakian T. G., Klessen R. S., Beck R., Spaans M., 2010, *A&A*, 522
- Schober J., Schleicher D., Federrath C., Glover S., Klessen R. S., Banerjee R., 2012, *ApJ*, 754
- Schober J., Schleicher D. R. G., Klessen R. S., 2013, *A&A*, 560
- Shang C., Bryan G. L., Haiman Z., 2010, *MNRAS*, 402, 1249
- Smith B., Regan J., Downes T., Norman M., O'Shea B., Wise J., 2018, *ArXiv e-prints*:1804.06477
- Smith B. D. et al., 2017, *MNRAS*, 466, 2217
- Stacy A., Greif T. H., Bromm V., 2010, *MNRAS*, 403, 45
- Stacy A., Greif T. H., Bromm V., 2012, *MNRAS*, 422, 290
- Sugimura K., Omukai K., Inoue A. K., 2014, *MNRAS*, 445, 544
- Sugimura K., Hosokawa T., Yajima H., Inayoshi K., Omukai K., 2018, *ArXiv e-prints*
- Sur S., Schleicher D. R. G., Banerjee R., Federrath C., Klessen R. S., 2010, *ApJ*, 721, L134
- Tremmel M., Governato F., Volonteri M., Pontzen A., Quinn T. R., 2018, *ArXiv e-prints*
- Truelove J. K., Klein R. I., McKee C. F., Holliman II J. H., Howell L. H., Greenough J. A., 1997, *ApJ*, 489, L179+
- Truelove J. K., Klein R. I., McKee C. F., Holliman II J. H., Howell L. H., Greenough J. A., Woods D. T., 1998, *ApJ*, 495, 821
- Tseliakhovich D., Hirata C., 2010, *Phys. Rev. D*, 82, 083520
- Turk M. J., Abel T., O'Shea B., 2009, *Science*, 325, 601
- Turk M. J., Smith B. D., Oishi J. S., Skory S., Skillman S. W., Abel T., Norman M. L., 2011, *ApJS*, 192, 9
- Turk M. J., Oishi J. S., Abel T., Bryan G. L., 2012, *ApJ*, 745, 154
- Visbal E., Haiman Z., Bryan G. L., 2014, *MNRAS*, 445, 1056
- Volonteri M., 2010, *A&A Rev.*, 18, 279
- Walmsley M., 1995, in *Revista Mexicana de Astronomia y Astrofisica Serie de Conferencias*, Vol. 1, *Circumstellar Disks, Outflows and Star Formation*, Cozumel, Mexico, Nov 28-Dec 2, 1994, p. 137. Vol. 1, p. 137
- Wang F. et al., 2016, *ApJ*, 819, 24
- Wang F. et al., 2017, *ApJ*, 839, 27
- Whalen D., Abel T., Norman M. L., 2004, *ApJ*, 610, 14
- Wise J. H., Abel T., 2011, *MNRAS*, 414, 3458
- Wise J. H., Turk M. J., Abel T., 2008, *ApJ*, 682, 745
- Wolcott-Green J., Haiman Z., 2012, *MNRAS*, 425, L51
- Wolcott-Green J., Haiman Z., Bryan G. L., 2011, *MNRAS*, 418, 838
- Woods T. E., Heger A., Whalen D. J., Haemmerlé L., Klessen R. S., 2017, *ApJ*, 842, L6

This paper has been typeset from a  $\text{\TeX}/\text{\LaTeX}$  file prepared by the author.